Nuclear reaction dynamics in $^{12}C + ^{120}Sn$ collisions

L. Garrido-Gómez, J. P. Fernández-García, and M. A. G. Alvarez
Departamento FAMN, Universidad de Sevilla, Apartado 1065, 41080 Sevilla, Spain

L. M. Martinis, J. K. L. Chaves, W. A. Y. Hatano, V. Scarduelli, L. R. Gasques, and L. C. Chamon
Instituto de Fisica, Universidade de São Paulo, Rua do Matão 1371, 05508-090 São Paulo, Brazil

J. Gomez, B. Paes, and A. Arazi
Laboratorio TANDAR, Comisión Nacional de Energía Atómica, BKNA 1650 Buenos Aires, Argentina and Consejo Nacional de Investigaciones Científicas y Técnicas, C1425FQB Buenos Aires, Argentina

(Received 19 March 2025; revised 12 September 2025; accepted 14 October 2025; published 2 December 2025)

Background: After two decades of systematic optical model (OM) analyses [L. C. Chamon *et al.*, Phys. Rev. C **66**, 014610 (2002); M. A. G. Alvarez *et al.*, Nucl. Phys. A **723**, 93 (2003); M. A. G. Alvarez *et al.*, Nucl. Phys. A **753**, 83 (2005); M. A. G. Alvarez *et al.*, Phys. Rev. C **100**, 064602 (2019); L. Garrido-Gómez *et al.*, Phys. Rev. C **109**, 054608 (2024); M. A. G. Alvarez *et al.*, Phys. Rev. C **103**, 054614 (2021)], a protocol has been developed to establish a common framework for describing reactions involving both tightly and weakly bound stable nuclei. This protocol involves applying different variants of OM, based on the double-folding São Paulo potential, along with the corresponding optical potentials (OP), to predict and/or reproduce experimental nuclear reaction data.

Purpose: The present work provides new data and theoretical calculations on the angular distributions of elastic scattering of $^{12}C + ^{120}Sn$ and the following nuclear reaction channels: inelastic excitations to the 2^+ state at 1171.27(2) keV and to the 3^- state at 2400.30(5) keV of the ^{120}Sn target, ^{12}C one-proton stripping $^{120}Sn(^{12}C, ^{11}B)^{121}Sb$, and one-neutron pickup $^{120}Sn(^{12}C, ^{13}C)^{119}Sn$ transfer reactions. The data were obtained at two bombarding energies: one below ($E_{lab} \approx 39$ MeV) and one above ($E_{lab} \approx 47$ MeV) the Coulomb barrier ($V_B \approx 42$ MeV).

Method: We perform OM calculations and compare them with the experimental data. The corresponding OP, based on the SPP, is determined. The OP, obtained from the elastic scattering analysis, is applied to the nuclear reaction calculations. Theoretical coupled channels and coupled reaction channels calculations are compared with the data.

Results: The analysis using the so-called São Paulo optical model protocol (SP-OMP) provides a better understanding of the dynamics of nuclear reactions as a function of bombarding energy and nuclear density models of ^{12}C. The SP-OMP effectively describes the elastic scattering cross sections of $^{12}C + ^{120}Sn$, with results consistent with previous systematic studies [M. A. G. Alvarez *et al.*, Nucl. Phys. A **723**, 93 (2003); M. A. G. Alvarez *et al.*, Phys. Rev. C **100**, 064602 (2019)]. The angular distributions related to the $^{12}C + ^{120}Sn$ inelastic excitations and nucleon transfer reactions are very well described by the coupling scheme of the theoretical calculations. Thus, we verified the contribution of each individual inelastic channel to reproduce the elastic scattering angular distributions. Comparisons of $^{12}C + ^{119,120}Sn$ are proposed.

Conclusion: The determined OP applied to microscopic nuclear reaction coupled-channel calculations represents a powerful tool for a consistent analysis of nuclear reactions.

DOI: 10.1103/p2cw-ls2j

I. INTRODUCTION

The ^{12}C nucleus is a stable isotope composed of a triple-α (^4He) cluster, exhibiting a higher binding energy per nucleon ($BE/A = 7680.14460(20)$ keV) than ^4He ($BE/A = 7073.91560(20)$ keV). The ^{12}C nucleus has a 2^+ excited state at 4439.82(21) keV and the 0^+ Hoyle state at 7654.07(19) keV, which lies above the α-particle separation energy ($Q_\alpha = 7366.59(4)$ keV) [1]. The existence of this state was first proposed by Hoyle in 1954 [2] and was experimentally confirmed a few years later by Cook *et al.* [3]. The ^{12}C ground state has a lower energy, which makes the probability of ^8Be capturing a ^4He nucleus extremely low and the formation of ^{12}C highly unlikely. To reach a stable configuration, the Hoyle state resonance is an intermediate step. The Hoyle state in the excited ^{12}C nucleus is the cornerstone of carbon formation in stellar environments, and ^{12}C itself is a fundamental element for the existence of life. Understanding the ^{12}C nucleus can provide new insights into nuclear forces, structure, and reactions [4].

The ^{120}Sn nucleus is a stable isotope of tin. It has excited states 2^+, at 1171.265(15) keV; the triplet 0^+, at 1875.108(25)

keV, 2^+, at 2097.205(20) keV, and 4^+, at 2194.299(21) keV; and 3^-, at 2400.30(5) keV [5], among many others.

Since 1954, when Feshbach [6,7] proposed the optical model (OM) as the simplest mathematical approach to describe nuclear reactions, a comprehensive general description remains elusive. Various OM approaches have been employed for the real and imaginary components of the optical potential (OP) to reproduce a vast amount of elastic scattering data involving both single nucleons and complex heavy ions over a wide energy range [8–18]. However, no single model has been able to fully account for nuclear structure, binding and bombarding energy dependencies, Coulomb-nuclear interference, the threshold anomaly, the dispersion relation, and other related effects [12,16].

In particular, some studies [8,9,19–23] have reported anomalies in OM analyses of reactions involving weakly bound nuclei, attributing them to the breakup process. These anomalies result in arbitrary variations of OP parameters and/or renormalizations of OP terms to fit experimental data, highlighting the need for more realistic OP approaches. Within this context, the nonlocal double-folding São Paulo potential (SPP) was developed to describe the real part of the nucleus–nucleus interaction [24–28]. In Ref. [29], the same SPP form factor was assumed for both the real and imaginary terms of the OP to describe reactions involving stable, tightly bound nuclei, over a wide energy range. This approach enabled a reasonable parameter-free description of the data set. The imaginary term was determined phenomenologically, despite lacking a formal theoretical justification for its energy dependence. Nevertheless, the results suggested that such a parameter-free model could provide realistic estimates for heavy-ion elastic scattering and reaction cross sections. Building on these findings, efforts were made to extend this approach to describe reactions involving stable weakly bound and exotic nuclei [30–33]. In particular, Refs. [31–33] further discuss the OP variations and link them with the projectile structure. In Ref. [31], we reported a systematic OM analysis of the elastic scattering angular distributions for ^{4,6}He, ^{6,7}Li, ^{9}Be, ^{10}B, and ^{16,18}O projectiles on ^{120}Sn targets at energies near their respective Coulomb barriers. In Ref. [32], we extended this study by analyzing the experimental elastic scattering angular distributions of ^{4,6}He, ^{6,7}Li, ^{9,10,11}Be, and ^{8}B impinging on ^{64}Zn targets. In addition, in Ref. [32], we compared results obtained with the different (^{64}Zn, ^{120}Sn) targets. A further test of consistency was also proposed for the ^{80}Se target. In Ref. [33], polarization effects were explicitly and successfully accounted for describing and comparing stable tightly and weakly bound with exotic nuclei (as projectiles) reacting on heavy targets. Using the aforementioned data sets, we reported theoretical OM calculations and the corresponding OP, based on the first (SPP) and second (SPP2) versions of the double-folding São Paulo potential [31,32]. This led to the development of the São Paulo Optical Model Protocol (SP-OMP). With the SP-OMP, we analyzed the sensitivity of the data fit to the OM calculations and variations in OP strengths and form factors. The OP was shown to be correlated with the projectile structure, its binding energy, and its dissociation(s) process(es) at scattering energies near the Coulomb barrier [31,32].

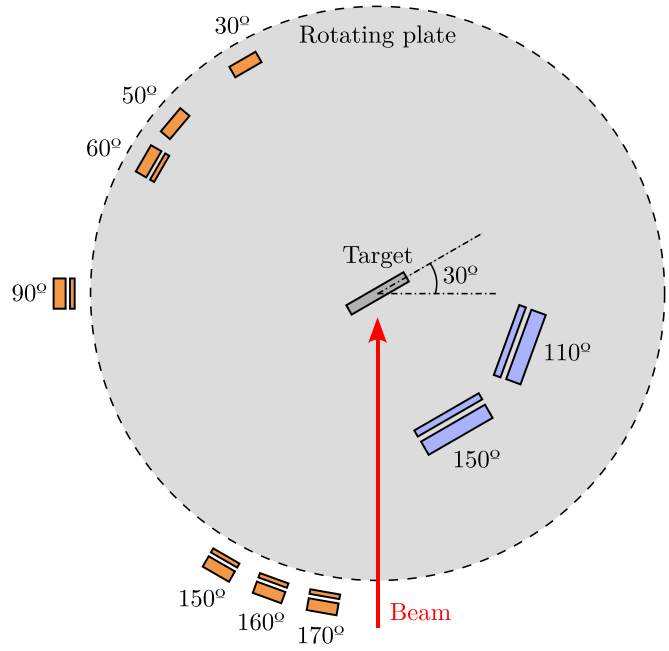

FIG. 1. Schematic representation of the experimental setup.

In this manuscript, we present new experimental data of the ^{12}C + ^{120}Sn nuclear reactions. In Sec. II, we describe the setup of the experimental campaign on ^{12}C + ^{119}Sn [34] and ^{12}C + ^{120}Sn (this work). In Sec. III, we apply the SP-OMP to study the elastic scattering angular distributions of ^{12}C + ^{120}Sn. In Sec. IV, we present the ^{12}C + ^{120}Sn nuclear reaction data compared to microscopic coupled channel (CC) calculations. A comparison between ^{12}C + ^{119,120}Sn is proposed in Sec. V A. In Sec. V B, we compare the critical and absorption distances of ^{12}C + ^{120}Sn with the ones of several systems. Finally, in Sec. VI, we summarize and present our main conclusions.

II. EXPERIMENTAL SETUP

The ^{12}C + ^{119,120}Sn experimental campaign was conducted at the Open Laboratory of Nuclear Physics and Applications at the University of São Paulo (LAFNA-USP, acronym in Portuguese), Brazil [34]. The 8 MV Pelletron accelerator provided ^{12}C ion beams at two bombarding energies: one below ($E_{\rm lab} \approx 39$ MeV) and one above ($E_{\rm lab} \approx 47$ MeV) the Coulomb barrier ($V_B \approx 42$ MeV). Two targets, ^{120}Sn and ^{120}Sn + ^{197}Au, each containing approximately 300 μg/cm^2 of ^{120}Sn, were used, tilted at 30° relative to the beam direction. In the latter, a 50 μg/cm^2 gold layer was evaporated for normalization purposes. Taking the target thicknesses into account, the laboratory energies measured at the center of the ^{120}Sn targets are $E_{\rm lab} = 38.7$ MeV and $E_{\rm lab} = 46.7$ MeV.

Figure 1 illustrates the experimental setup. It was assembled in the scattering chamber of the 30B experimental beamline at the LAFNA-USP facility.

The detection system consisted of two single silicon (Si) surface barrier detectors (SBD) positioned at $\theta_{\rm lab} = 30°$ and

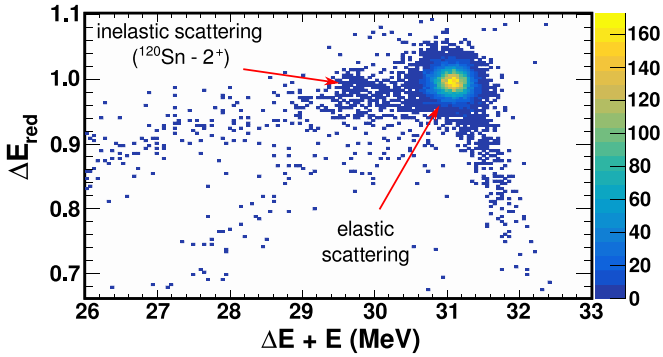

FIG. 2. ^{12}C + ^{120}Sn spectrum measured at E_{lab} = 38.7 MeV and $\theta_{lab} = 89.3°$. ΔE_{red} is a normalized energy unit used to conveniently plot the sum of the yields from different pixels without compromising resolution (see text for details).

50°, primarily for normalization purposes, and five Si SBD telescopes placed at $\theta_{lab} = 60°$, 90°, 150°, 160°, and 170°. The two single Si SBDs and the telescope at $\theta_{lab} = 60°$ were positioned 25 cm from the target and mounted on a rotating plate. The remaining Si SBD telescopes were placed 30 cm from the target and mounted on fixed supports. Additionally, the detection system STAR (silicon telescopes array for reactions) was installed. STAR consists of two large-area telescopes (50 × 50 mm^2), each composed of two 20 μm single-sided silicon strip detectors (SSSSD), segmented into 16 vertical strips, serving as ΔE detectors, and two 300 μm SSSSD detectors, segmented into 16 horizontal strips, serving as E detectors. The two telescopes were mounted on the rotating plate and positioned 11 cm from the target. With its rotational capability, STAR can cover an angular range from $\theta_{lab} \approx 84°$ to ≈161°. Further details on the experiment, including the STAR detection system and its characterization, can be found in Ref. [34]. To improve the statistical precision of the measurements, we sum the yields measured from a single vertical strip of the front (ΔE) detector with those from the corresponding 16 horizontal strips of the back (E) detector, effectively forming 16 pseudo-telescopes. Due to angular variation in the ϕ direction, this procedure results in an angular spread of approximately 1°, which varies slightly with the scattering angle θ. Summing the yields of pixels with slightly different thicknesses can compromise the resolution of the spectra. To avoid this, we use the quantity ΔE_{red}, defined as the ratio of experimental to calculated energy loss (see Ref. [34])

Figure 2 presents a bidimensional (ΔE_{red} versus $\Delta E + E$) spectrum of the ^{12}C + ^{120}Sn reaction, obtained at E_{lab}=38.7 MeV and $\theta_{lab} = 89.3°$, with the STAR telescope covering intermediate angles. From Fig. 2, obtained with a pure ^{120}Sn target, inelastic excitations can be observed in addition to elastic scattering.

Figure 3 presents bidimensional spectra obtained at E_{lab}=46.7 MeV and $\theta_{lab} = 104.3°$. In Fig. 3(a), we identify events corresponding to the elastic scattering of ^{12}C in ^{120}Sn and ^{197}Au, the latter being used for normalization purposes. In Fig. 3(b), obtained with a pure ^{120}Sn target, we identify events associated with the elastic scattering of ^{12}C and inelastic excitations to the 2$^+$ state at 1171.265(15) keV and the 3$^-$ state at 2400.30(5) keV of the ^{120}Sn target. Additionally, we observe the one-neutron pickup transfer reaction, ^{120}Sn(^{12}C, ^{13}C) ^{119}Sn, and the Z = 5 band, associated with the one-proton stripping transfer reaction, ^{120}Sn(^{12}C, ^{11}B) ^{121}Sb.

III. OPTICAL MODEL

A. Theoretical approach

The elastic scattering cross sections of ^{12}C + ^{120}Sn at E_{lab} = 38.7 and 46.7 MeV have been studied within the OM framework. The models described below adopt a complex OP approach to represent the nuclear interaction, given by

$$U_N(R) = V(R) + iW(R), \quad (1)$$

where $V(R)$ and $W(R)$ denote the real and imaginary components, respectively.

The real term of the OP is described using the updated version of the São Paulo potential (SPP2), as presented in Ref. [35]. This potential is defined as

$$V_{SPP2}(R) = \iint U_0\, \rho_1(\vec{r}_1)\rho_2(\vec{r}_2)\, e^{-(r/a)^2} e^{-4v^2/c^2} d\vec{r}_1 d\vec{r}_2. \quad (2)$$

Here ρ_1 and ρ_2 represent the matter distributions of the projectile and target, respectively; v is the relative velocity between them; c is the speed of light; and $r = |\vec{R} - \vec{r}_1 + \vec{r}_2|$. The

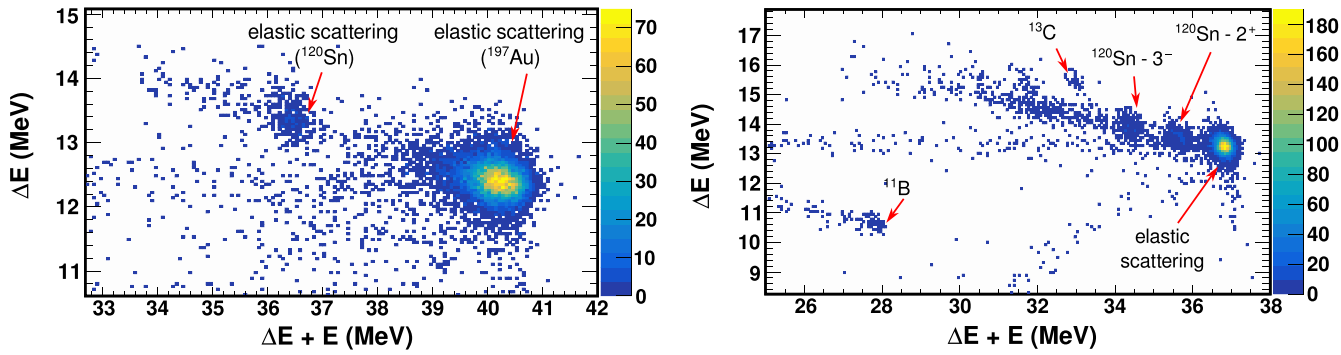

(a) (b)

FIG. 3. Spectra of (a) ^{12}C + ^{120}Sn, ^{197}Au and (b) ^{12}C + ^{120}Sn measured at E_{lab} = 46.7 MeV and $\theta_{lab} = 104.3°$.

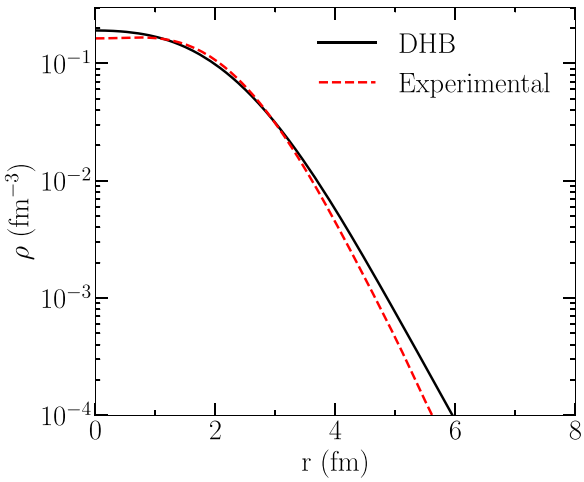

FIG. 4. Nuclear matter densities for ^{12}C. The solid line represents the theoretical calculation obtained using the DHB model [36]; the dashed line corresponds to the experimental density derived from electron scattering measurements [37].

parameters are given by $U_0 = -735.813$ MeV and $a = 0.50$ fm.

Equation (2) is computed by the `REGINA` code [35]. It relies on theoretical nuclear densities from the Dirac-Hartree-Bogoliubov (DHB) model [36] or experimental nuclear densities from electron scattering experiments [37].

Figure 4 presents two different approaches to the matter density of ^{12}C. The dashed line represents the experimental density, while the solid line corresponds to the theoretical DHB density. The matter density of ^{120}Sn is obtained from the DHB model.

Substituting Eq. (2) in Eq. (1), we propose four OM variants that define what we call the protocol (SP-OMP) and account for different physical phenomena, as follows.

(i) OM1: considers only the internal absorption of flux due to barrier penetration, following the OP approach:

$$U_N(R) = V_{\rm SPP2}(R) + iW(R), \tag{3}$$

where $W(R)$ is a Woods-Saxon-type potential,

$$W(R) = W_0/[1 + \exp((R - R_0)/a)], \tag{4}$$

with $W_0 = -100$ MeV, $R_0 = r_0(A_1^{1/3} + A_2^{1/3})$, $r_0 = 1.06$ fm, and $a = 0.25$ fm [31,32]. The small values of diffusivity and reduced radius are appropriate for simulating only the fusion process and do not account for transitions to other peripheral nonelastic channels.

The next three variants assume the SPP2 potential Eq. (2) for both the real and imaginary terms of the OP, given by

$$U_N(R) = N_r V_{\rm SPP2}(R) + iN_i V_{\rm SPP2}(R). \tag{5}$$

N_r and N_i are normalization factors that determine the strengths of each term and provide a simple way to simulate the effects of the polarization potential. This polarization arises from nonelastic couplings and, according to Feshbach theory [6,7], is both energy-dependent and complex. The imaginary term originates from transitions to open nonelastic channels, which absorb flux from the elastic channel. The real term, in turn, results from both real and virtual transitions to intermediate states, such as inelastic excitations or nucleon transfer.

(ii) OM2: uses the SPP2 approach for the real and imaginary terms of the OP [Eq. (5)], with the normalization factors fixed at standard values: $N_r = 1$ and $N_i = 0.78$. Elastic scattering angular distributions for many stable, tightly bound nuclei have been successfully described using this model [29].

(iii) OM3: Employs the same OP approach as OM2, with $N_r = 1.0$ [Eq. (5)]. However, the N_i factor is allowed to vary to fit experimental data. A systematic study of light cluster-structured nuclei reactions was conducted within the OM3 approach [31,32]. It showed a sharp increase in the N_i value at scattering energies, close to the sum of the Coulomb barrier of the system and the projectile breakup (cluster dissociation) Q value [32].

(iv) OM4: uses the same OP as OM2 and OM3 [Eq. (5)], with both N_r and N_i allowed to vary to fit the experimental data.

The OM calculations were performed using the `FRESCO` code and its routine `SFRESCO` [38]. It is worth mentioning that the OM1 and OM2 variants of the SP-OMP do not have adjustable parameters. Therefore, they can be considered as theoretical predictions, while OM3 and OM4 correspond to data fits. The uncertainties on the OM3 and OM4 parameters are determined by assuming the $\chi^2_{\rm min}$ variation of $\chi^2_{\rm min}/N$ for the OM3 case (one parameter, N_i fit) [32], and $2.35(\chi^2_{\rm min}/N)$ for the OM4 case (two parameters, N_r and N_i fit) [39], where N is the number of experimental data points. Thus, we assume the standard deviation to determine the confidence interval (1σ) of the fit parameters.

It is worth mentioning that this protocol was recently used for the first time in Ref. [32]. It was applied for a systematic study on weakly bound nuclei reactions. Such a protocol showed the need to vary the OP parameters (specifically related to the OP strengths). Unlike what happens for tightly bound nuclei (as it is the case for ^{12}C), for weakly bound nuclei the real OP strength is surpassed by the imaginary one in the energy range around and above the Coulomb barrier (with a strong correlation between the real and imaginary OP strengths and sensitivity of the data to their choice). Thus, despite their simplicity, the best-fit OP parameters correlated with the weakly bound structure of the projectile and pointed to a systematic increase of weakly bound nuclei reactions.

B. Optical model analysis

Tables I and II present the SP-OMP parameters and $\chi^2_{\rm red}$ of ^{12}C + ^{120}Sn data fit, at $E_{\rm lab} = 38.7$ MeV (Table I) and 46.7 MeV (Table II). In these tables, we present results applying both the DHB and the experimental model (see Fig. 4) for the ^{12}C nuclear matter density [35–37].

Figures 5 and 6 present elastic scattering angular distributions of ^{12}C + ^{120}Sn, at 38.7 and 46.7 MeV. Figure 5 presents the theoretical predictions obtained with OM1 and OM2.

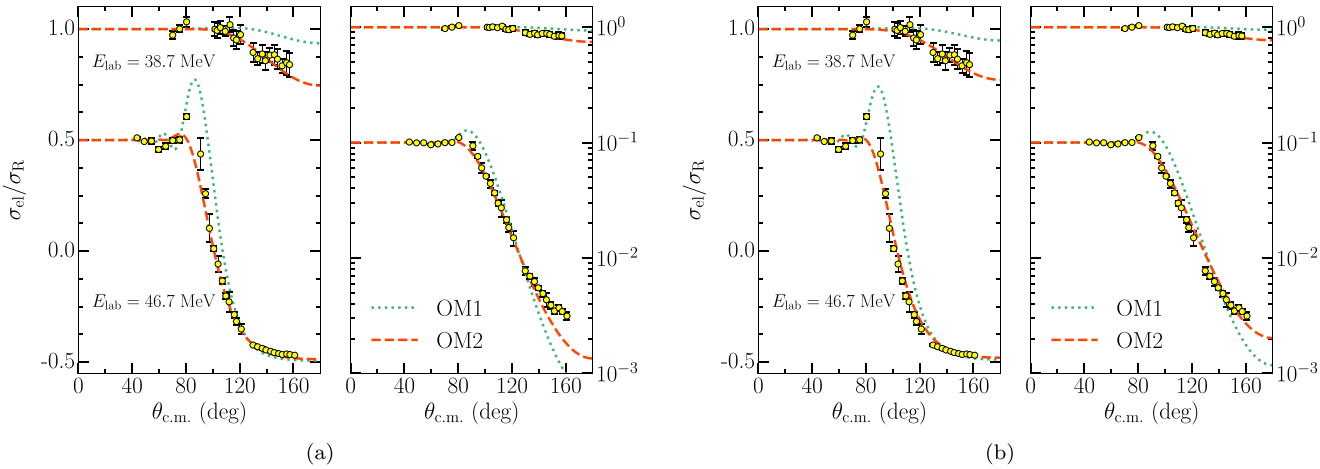

FIG. 5. Elastic scattering angular distributions of $^{12}C + ^{120}Sn$ in linear scale (left) and logarithmic scale (right). The curves represent the cross sections obtained with OM1 (dotted green) and OM2 (dashed red). For comparison, data for $E_{lab} = 46.7$ MeV have been shifted by a constant factor. (a) Calculations with theoretical (DHB) density [36] and (b) Calculations with experimental density [37].

Figure 6 presents data fit obtained with OM3 and OM4. In both Figs. 5 and 6, we apply the DHB and the experimental nuclear matter densities of ^{12}C (Fig. 4) [35–37] in the calculations.

At the energy below the Coulomb barrier ($E_{lab} = 38.7$ MeV), OM1 does not reproduce the data set. This discrepancy is likely related to the peripheral inelastic excitations observed in Fig. 2, which are not accounted for by the internal potential approach of OM1. Unlike OM1, the other variants OM2, OM3, and OM4 fit the experimental data quite well, regardless of the model applied to the ^{12}C nuclear matter density. From Table I, the fixed parameter values of OM2 are compatible with the adjusted values obtained with OM3 and OM4; $\chi^2_{red} < 1.0$ is obtained for all three cases. Moreover, analyzing the results of OM4, the data show much greater sensitivity to the imaginary than to the real OP term (see the error bars in Table I).

At the energy above the barrier ($E_{lab} = 46.7$ MeV), the OM1 prediction shows a pronounced disagreement with the experimental data. This disagreement is especially evident at forward angles, near the Coulomb-nuclear interference peak. This behavior is expected, as this model only accounts for barrier penetration (internal absorption) and does not include peripheral reaction channels.

In Fig. 5, compared to OM1, a better description of the $^{12}C + ^{120}Sn$ data at 46.7 MeV is achieved with OM2. However, OM2 tends to suppress the Coulomb-nuclear interference (rainbow) at forward angles ($\sim 80^\circ$). The data trend is better described by OM3 and OM4 (see Fig. 6 and Table II).

Analyzing the results obtained with the DHB model for the ^{12}C matter density, OM4 yield the best value of χ^2_{red}, which is slightly better than those obtained with OM2 and OM3. However, the parameters N_r and N_i obtained with OM4 are compatible with those of OM2 and OM3, within the respective uncertainties (up to 3σ).

By comparing the values presented in Tables I and II, we can note that the uncertainties of the normalization factors at the lower energy are larger than those at the higher energy, particularly with respect to the N_r factor. In fact, the low-energy data appear to be quite insensitive to the real OP term.

TABLE I. OM parameters for $^{12}C + ^{120}Sn$ at $E_{lab} = 38.7$ MeV. (a) Calculations with the DHB model for the ^{12}C nuclear matter density [36]. (b) Calculations with experimental model for the ^{12}C nuclear matter density [37].

	N_r	N_i	χ^2_{red}
(a)			
OM1	1	—	4.4
OM2	1	0.78	0.51
OM3	1	0.82 ± 0.07	0.51
OM4	0.71 ± 0.87	0.89 ± 0.22	0.50
(b)			
OM1	1	—	4.5
OM2	1	0.78	0.55
OM3	1	0.86 ± 0.07	0.52
OM4	1.23 ± 0.91	0.81 ± 0.21	0.52

TABLE II. Same as Table I at $E_{lab} = 46.7$ MeV. (a) Calculations with the DHB model for the ^{12}C nuclear matter density [36]. (b) Calculations with experimental model for the ^{12}C nuclear matter density [37].

	N_r	N_i	χ^2_{red}
(a)			
OM1	1	—	89
OM2	1	0.78	12
OM3	1	0.64 ± 0.06	9.9
OM4	0.90 ± 0.04	0.73 ± 0.06	7.5
(b)			
OM1	1	—	169
OM2	1	0.78	11
OM3	1	0.93 ± 0.06	9.3
OM4	1.10 ± 0.05	0.79 ± 0.06	7.5

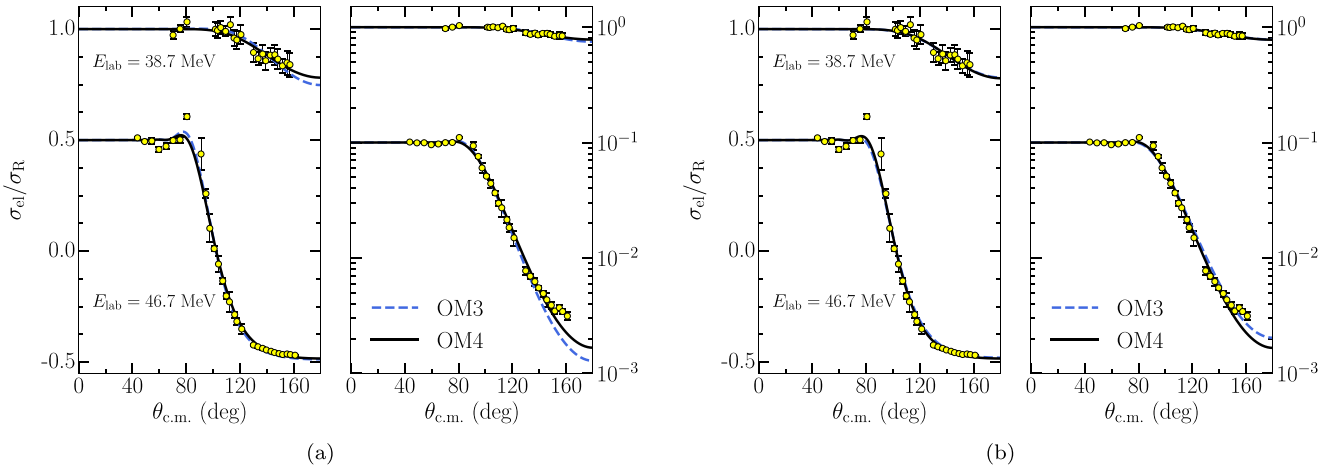

FIG. 6. Same as in Fig. 5, but with OM3 (dashed blue) and OM4 (solid black) fits. (a) Calculations with theoretical (DHB) density [36] and (b) Calculations with experimental density [37].

From Fig. 6, we observe that the OM3 and OM4 calculations, performed with the DHB model for the ^{12}C matter density, provide equivalent data fits. OM3 calculations, with the experimental model applied to the ^{12}C nuclear matter density, provide a better fit at backward angles and a worse fit at forward angles (rainbow region).

The lack of experimental matter densities for some nuclei and the good results provided by the DHB model, conducted using the latter for our systematics [31,32].

Comparing the results obtained by applying the parameter-free OM2 with those obtained by varying the parameter(s) in OM3 and OM4, the latter OM variants better account for the open reaction channels observed in Fig. 3(b). The results of χ^2_{red}, presented in Table II, support this conclusion.

Figure 7 illustrates the variation of χ^2_{red} as a function of the OM4 fit parameters for $^{12}C + ^{120}Sn$ data, at 38.7 MeV [Fig. 7(a)] and 46.7 MeV [Fig. 7(b)].

At the lower energy (38.7 MeV), the data show very low sensitivity to the real term and greater sensitivity to the imaginary term of the OP.

At the higher energy (46.7 MeV), the data show sensitivity to both the real and imaginary OP terms. In Fig. 7, the OM2 fixed parameters ($N_r = 1.0$ and $N_i = 0.78$) and its consequent theoretical prediction are consistent with the best χ^2_{red} region. Additionally, we can observe the correlation between the N_r and N_i values: larger N_r values require smaller N_i values to fit the data. This is corroborated by the negative correlation factors, obtained from the OM4 fit, at 38.7 MeV and 46.7 MeV, which are -0.892 and -0.584, respectively. Finally, in Table III, we present the total reaction cross sections for $^{12}C + ^{120}Sn$ at 38.7 and 46.7 MeV, obtained with OM3. As expected, the higher the energy, the higher the total reaction cross section.

IV. COUPLED CHANNEL CALCULATIONS

The nuclear reaction cross sections of $^{12}C + ^{120}Sn$ at $E_{lab} = 46.7$ MeV have been studied within the microscopic coupled (reaction) channel (CC and CRC) calculations. In addition to the $^{12}C + ^{120}Sn$ elastic scattering process, we observed

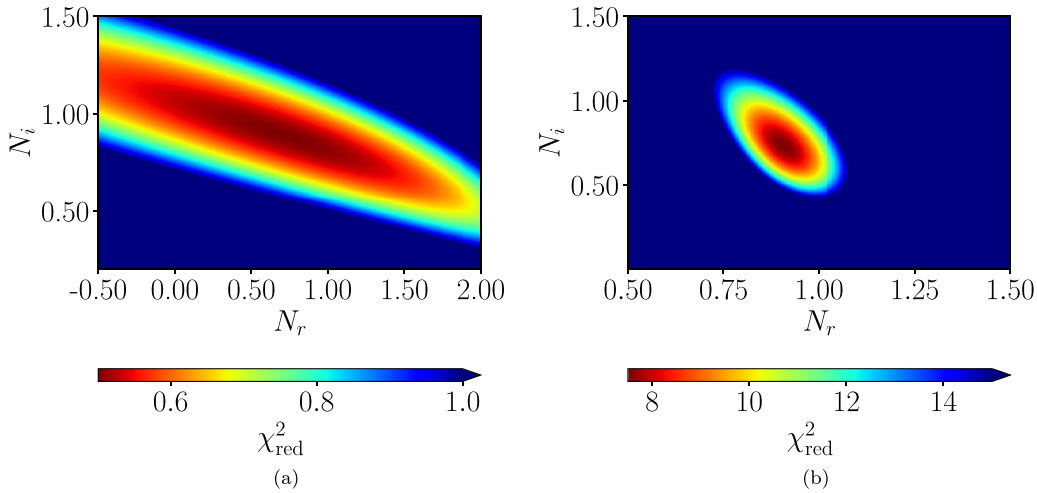

FIG. 7. χ^2_{red} as a function of the OM4 (N_r and N_i) fit parameters for the $^{12}C + ^{120}Sn$ reaction. (a) $E_{lab} = 38.7$ MeV and (b) $E_{lab} = 46.7$ MeV.

TABLE III. Total reaction cross sections for the $^{12}C + ^{120}Sn$, at 38.7 and 46.7 MeV, obtained with the OM3.

	38.7 MeV	46.7 MeV
$^{12}C + ^{120}Sn$	(51 ± 5) mb	(509 ± 14) mb

the following nuclear reactions: inelastic excitations to the 2^+ and 3^- states of the ^{120}Sn target at 1171.27(2) keV and 2400.30(5) keV, respectively, and the inelastic excitations to the 2^+ state of the ^{12}C projectile, at 4439.8(2) keV; the ^{12}C one-proton stripping transfer, ^{120}Sn(^{12}C, ^{11}B)^{121}Sb [$Q = -10166(3)$ keV] and the ^{12}C one-neutron pickup transfer, ^{120}Sn(^{12}C, ^{13}C)^{119}Sn [$Q = 1223.9(13)$ keV]. The above-mentioned Q values are obtained from Ref. [1].

A. Inelastic excitations

The CC calculations were performed using the FRESCO code [38]. The OP are applied as the initial interaction to calculate the angular distributions of inelastic excitations and nucleon transfer reactions. These calculations apply SPP2 for the real term of the nuclear interaction [35]. For the imaginary part of the OP, a phenomenological Woods-Saxon (WS) parametrization (OM1) was adopted, with parameters W_0= 100 MeV, r_{i0}=1.06 fm, and a_i= 0.25 fm [32].

With the OM1 approach, the strength of the imaginary potential in the surface region is negligible, accounting only for internal flux absorption due to barrier penetration. Thus, the OM1 approach simulates the small fusion process, and it does not take into account transitions to the other peripheral nonelastic channels.

The coupling scheme includes the 2^+ and 3^- excited states of the ^{12}C projectile, at 4439.8(2) and 9641(5) keV; the 2^+ and 3^- excited states of the ^{120}Sn target, respectively, at 1171.27(2) keV and 2400.30(5) keV, in addition to the 2^+ states at 2728.12(3), 2930.53(5), 3157.97(9), and 3547.58(19) keV. The last four states produce negligible effects on the calculations. The Hoyle state of ^{12}C at 7654 keV has no direct transition to the 0^+ ground state and, hence, was not considered in these calculations [34].

Table IV presents the spin, excitation energy (E^*), transition mode (λ), Coulomb transition probability [$B(E\lambda)$], and deformation length (δ_λ) of the corresponding excited states. The nuclear deformation (δ_λ) values associated with the respective Coulomb transition probabilities [$B(E\lambda)$] were determined considering the effect of the finite diffuseness value of the nuclear density [43,44]. Figures 8 and 9 present the experimental and theoretical angular distributions of inelastic excitations of ^{120}Sn (2^+ at 1171.27(2) keV and 3^- at 2400.30(5) keV, respectively), bombarded by ^{12}C. The theoretical inelastic scattering angular distributions, obtained from the calculations, show considerable (not negligible) sensitivity to the coupling scheme. Thus, in Figs. 8 and 9, dashed lines represent calculations performed by coupling only the excited states of the target. The solid lines also include the projectile excitations to the coupling scheme. The values of

TABLE IV. Spin, excitation energies (keV), transition amplitudes from the g.s. to the excited states ($10^{-3}e^2b^\lambda$) and deformation lengths (fm), for the inelastic states included in the CC calculations. Values have been extracted from Refs. [1,45–47].

Nucleus	Spin	E^*	λ	$B(E\lambda)\uparrow$	δ_λ	Ref.
^{120}Sn	2^+	1171.27(2)	2	197.5	0.62	[45]
^{120}Sn	3^-	2400.30(5)	3	115	0.84	[46]
^{120}Sn	2^+	2728.12(3)	2	23.0	0.082	[1]
^{120}Sn	2^+	2930.53(5)	2	7.7	0.12	[1]
^{120}Sn	2^+	3157.97(9)	2	15.0	0.17	[1]
^{120}Sn	2^+	3547.58(19)	2	260.0	0.72	[47]
^{12}C	2^+	4439.8(2)	2	3.97	1.42	[1]
^{12}C	3^-	9641(5)	3	0.251	1.66	[1]

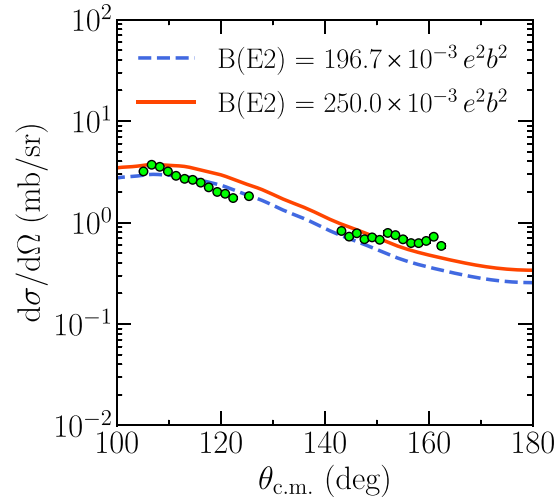

FIG. 8. Angular distributions of ^{120}Sn inelastic excitation (2^+, at 1171.27(2) keV [5]), bombarded by ^{12}C, at $E_{lab} \approx 46.7$ MeV. The lines represent theoretical calculations performed with different coupling schema (see Table IV and text for more details).

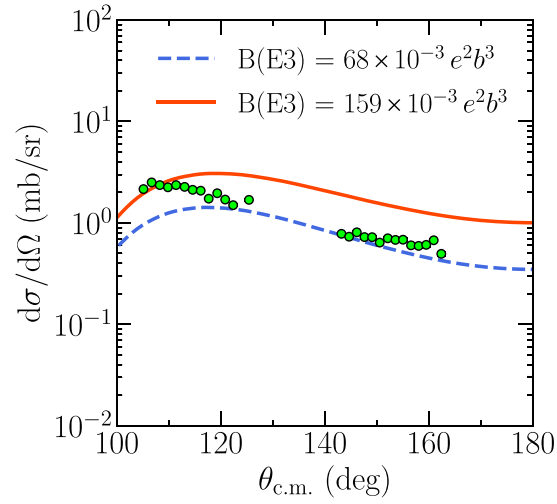

FIG. 9. Angular distributions of ^{120}Sn inelastic excitations (3^-, at 2400.30(5) keV [5]), bombarded by ^{12}C, at $E_{lab} \approx 46.7$ MeV. The lines represent theoretical calculations performed with different coupling schema (see Table IV and text for more details).

TABLE V. Spectroscopic factors for the one-neutron pickup and one-proton stripping transfer states.

Overlap	E* (MeV)	State (nlj)	C^2S_{lj}	Ref.
$\langle {}^{13}C \mid {}^{12}C+n\rangle$	0.00	$1p_{1/2}$	0.56	[34]
$\langle {}^{13}C \mid {}^{12}C+n\rangle$	0.00	$1p_{1/2}$	1.4	[42]
$\langle {}^{120}Sn \mid {}^{119}Sn+n\rangle$	0.00	$3s_{1/2}$	0.58	[48]
$\langle {}^{120}Sn \mid {}^{119}Sn+n\rangle$	0.02	$2d_{3/2}$	1.66	[48]
$\langle {}^{120}Sn \mid {}^{119}Sn+n\rangle$	0.09	$1h_{11/2}$	3.35	[48]
$\langle {}^{120}Sn \mid {}^{119}Sn+n\rangle$	0.79	$1g_{7/2}$	5.15	[48]
$\langle {}^{12}C \mid {}^{11}B+p\rangle$	0.00	$1p_{3/2}$	5.70	[40]
$\langle {}^{12}C \mid {}^{11}B+p\rangle$	0.00	$1p_{3/2}$	3.58	[41]
$\langle {}^{121}Sb \mid {}^{120}Sn+p\rangle$	0.00	$2d_{5/2}$	0.915	[49]
$\langle {}^{121}Sb \mid {}^{120}Sn+p\rangle$	0.04	$1g_{7/2}$	1.13	[49]
$\langle {}^{121}Sb \mid {}^{120}Sn+p\rangle$	0.51	$2d_{3/2}$	0.295	[49]
$\langle {}^{121}Sb \mid {}^{120}Sn+p\rangle$	0.57	$3s_{1/2}$	0.379	[49]

the ^{120}Sn deformation parameters were extracted from Refs. [45,46], according to Table IV.

B. One proton and one neutron transfer reactions

The experimental differential cross section for the one-proton stripping, ^{120}Sn(^{12}C, ^{11}B)^{121}Sb, and one-neutron pickup, ^{120}Sn(^{12}C, ^{13}C)^{119}Sn, have been obtained considering the ground states and different excited states of the residual nuclei, ^{121}Sb and ^{119}Sn, respectively (Table V). In the former, the calculations only take into account the one-proton stripping channel, while in the latter, a complete (full) CRC calculation was considered, according to Tables IV and V, to describe the data. The real term of SPP2 [35] was assumed for the corresponding particle-core potentials. The imaginary WS shape potential (OM1) was assumed to simulate internal flux absorption. The OM3 prescription obtained for ^{12}C + ^{120}Sn was assumed for the exit channel potentials (a significant change is not appreciated assuming OM2 instead of OM3 for the exit channel potentials). This common approach has provided a very good description of the different transfer channels.

Figures 10 and 11 present the experimental data and theoretical (CRC) calculations for the angular distributions of the ^{12}C one-proton stripping and one-neutron pickup transfer reactions.

Table V presents the spectroscopic factors for the ground states and excited states of the residual nuclei obtained from the literature.

In Figs. 10 and 11 a minimum and maximum value of the spectroscopic factors corresponding to the overlaps $\langle {}^{13}C \mid {}^{12}C+n\rangle$ and $\langle {}^{12}C \mid {}^{11}B+p\rangle$ are considered and represented by dashed (blue) and solid (red) lines. In Figs. 10 and 11, the better agreement between the data and the calculations is obtained with the maximum values of spectroscopic factor.

C. Influence of the inelastic excitations and transfer reactions on the elastic scattering

Figure 12 presents the elastic scattering angular distributions for the ^{12}C + ^{120}Sn system, measured at ∼46.7 MeV and compared to the theoretical calculations. In Fig. 12, the dotted line corresponds to the pure OM1 calculation without coupled channels. This OM1 is applied as the initial interaction to study the angular distributions of elastic scattering, inelastic excitations, and nucleon transfer reactions. From Fig. 12, we verify the contribution of coupling each inelastic excitation channel to reproduce the elastic scattering angular distributions of ^{12}C + ^{120}Sn at 46.7 MeV. These calculations progressively take into account the inelastic excitations to the ^{120}Sn 2^+ state, at 1171.27(2) keV (dashed line), and the 3^- state, at 2400.30(5) keV (dashed-dotted line). The calculations are carried out with the deformation parameters presented in

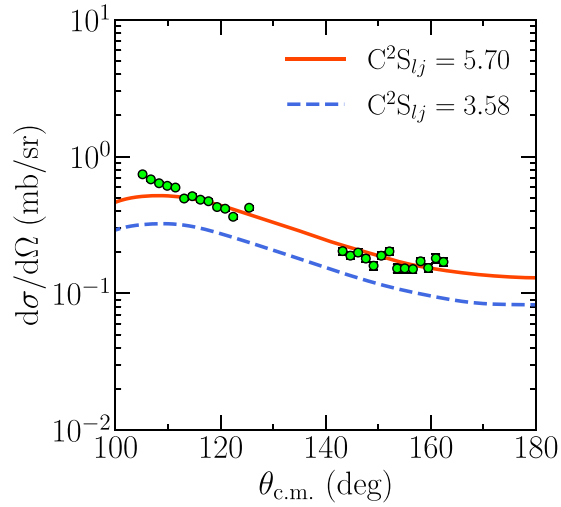

FIG. 10. Angular distributions of the ^{12}C one-proton stripping, ^{120}Sn(^{12}C, ^{11}B)^{121}Sb, at $E_{lab} \approx 46.7$ MeV. The lines represent theoretical calculations performed with two different values for the spectroscopic factor ([40,41]) of the projectile (see Table V and text for more details).

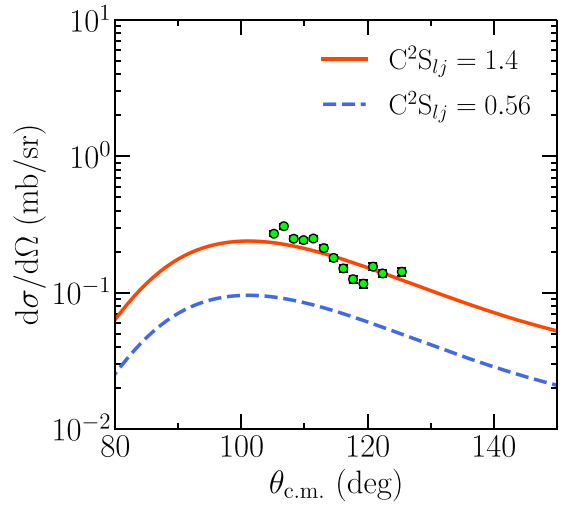

FIG. 11. Angular distributions of the ^{12}C one-neutron pickup ^{120}Sn(^{12}C, ^{13}C)^{119}Sn, transfer reactions, at $E_{lab} \approx 46.7$ MeV. The lines represent theoretical calculations performed with two different values for the spectroscopic factor [34,42] of the projectile (see Table V and text for more details).

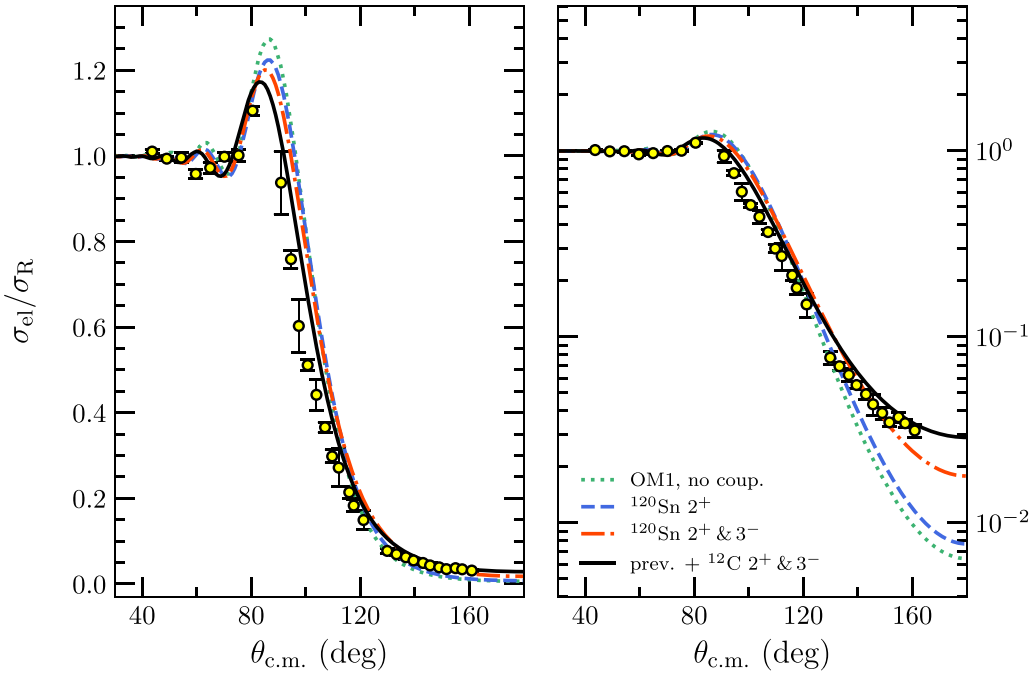

FIG. 12. Elastic scattering angular distributions, in linear (left) and logarithmic (right) scales, for the $^{12}C + ^{120}Sn$ systems, at $E_{lab} \approx 46.7$ MeV (see text for more details).

Table IV and extracted from Refs. [45,46]. In addition, the coupling scheme takes into account the inelastic excitations to the ^{12}C 2^+ and 3^- states, at 4439.8(2) and 9641(5) keV (solid line). We can observe that, as a new coupling is assumed, the agreement between the calculation and the elastic scattering data improves. After coupling the four excited states mentioned above (solid line), the match between calculations and data improves significantly. The effect of coupling other inelastic (Table IV) and transfer (Table V) channels is negligible. The results observed in Fig. 12 corroborate the results observed in Figs. 5 and 6, where the calculations with OM2 and OM3 account much better for the peripheral reaction (inelastic excitation) channels.

In the entrance channel, the OM1 potential, simulating internal flux absorption, was assumed. The OM3 prescription, obtained for the $^{12}C + ^{120}Sn$, was assumed for the exit channel potential. To study the role of the exit channel potential in the CRC calculations, we have also carried out calculations with the OM2 potential. No considerable effect on the ^{120}Sn(^{12}C, ^{11}B)^{121}Sb and ^{120}Sn(^{12}C, ^{13}C)^{119}Sn angular distributions was observed. In Fig. 12, an identical (best-fit) curve is obtained for the elastic scattering angular distribution when coupling the transfer and changing the exit potential from OM3 to OM2. It is quite expected from the OM analyses (Table II) and since the transfer couplings had no effect on the elastic channel. Furthermore, no considerable effect on the ^{120}Sn(^{12}C, ^{11}B)^{121}Sb and ^{120}Sn(^{12}C, ^{13}C)^{119}Sn angular distributions was observed.

Table VI presents the cross sections of different reaction channels obtained from the CRC calculations. The total reaction cross section ($\sigma_{total} = 409.4$ mb), obtained from the CRC calculations, can be compared to the same quantity obtained with the SP-OMP approach ($\sigma_{total} = 509 \pm 14$ mb) (see Table III). The differences can be understood by analyzing Fig. 6, at backward angles, where OM3 shows a certain disagreement ($\chi^2_{red} = 9.9$; see Table II) with the experimental data. Some other reaction channels, which have not been included in the coupling scheme, should contribute to this difference.

V. TESTS OF CONSISTENCY

A. Comparison of $^{12}C + ^{119,120}Sn$

As a further test of consistency, we compare the elastic scattering angular distributions (experimental data and theoretical calculations) of $^{12}C + ^{119}Sn$ [34] with $^{12}C + ^{120}Sn$ ones

TABLE VI. Cross sections of different reaction channels obtained from the CRC calculations for the $^{12}C + ^{119,120}Sn$ systems: σ_{ine}^{target} and σ_{ine} ^{12}C represent the inelastic scattering corresponding to the coupled excited states of the target and the projectile, respectively; σ_{1n} and σ_{1p} correspond to the neutron pickup and proton stripping transfer processes, respectively; σ_{abs} is the absorption cross section from the internal potential.

System	σ_{total} (mb)	σ_{ine}^{target} (mb)	σ_{ine} ^{12}C (mb)	σ_{1n} (mb)	σ_{1p} (mb)	σ_{abs} (mb)
$^{12}C + ^{120}Sn$	409.4	74.0	16.1	1.1	1.9	316.3
$^{12}C + ^{119}Sn$ [34]	464.7	127.3	9.1	3.6	1.5	323.2

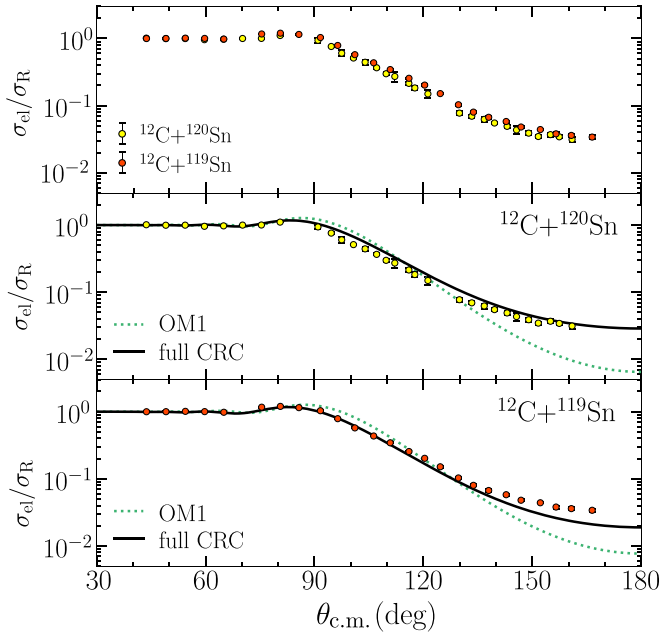

FIG. 13. Elastic scattering angular distributions for the $^{12}C+^{119}Sn$ [34] compared to $^{12}C+^{120}Sn$ (this work), at $E_{lab} \approx 47$ MeV (see text for more details).

(this work). Both systems were measured at a bombarding energy of ∼47 MeV.

Figure 13 presents the $^{12}C+^{119,120}Sn$ experimental data. The dotted lines correspond to pure OM1 calculations without coupled channels, and the solid lines correspond to the full coupling as described in Sec. IV C and represented in Fig. 12. In both cases, the combination of OM1 with CC calculations describes the experimental data fairly consistently.

In addition, we can compare the intensity of the different reaction channels by looking at the calculated cross sections in Table VI. The main difference is related to the inelastic scattering cross sections of the target, which can be associated with the higher density of low-lying states of ^{119}Sn with respect to ^{120}Sn. Unlike ^{120}Sn, the experimental cross sections of ^{119}Sn involve contributions from multiple excited states. In particular, couplings associated with the excitation of states near 2.30 MeV were experimentally observed and showed a significant effect on the elastic scattering description [34]. Further discussions are presented in Secs. V B and VI.

B. Critical and absorption distances

The present data are represented as a function of the semiclassical distance of closest approach and compared across different systems. This analysis identifies the distances at which the peripheral and fusion reaction channels are activated, providing critical information on the influence of the nuclear mass distribution and the binding strength, whether tightly or weakly bound, on the dynamics of the interaction and the resulting reaction mechanisms [50,51].

The distance of closest approach is calculated by

$$D = \frac{Z_p Z_T e^2}{2E_{CM}}(csc(\theta_{CM}/2) + 1), \quad (6)$$

TABLE VII. Calculated reduced critical interaction d_I and the reduced strong-absorption d_S distances presented in Ref. [50], for tightly and weakly bound projectiles reacting on ^{120}Sn.

System	Q_{bu} (MeV)	d_I (fm)	d_S (fm)	Ref.
$^{6}He+^{120}Sn$	0.975	2.60(8)	1.567(9)	[52]
$^{6}Li+^{120}Sn$	1.474	2.00(3)	1.555(5)	[31]
$^{9}Be+^{120}Sn$	1.655	1.94(2)	1.588(4)	[54]
$^{7}Li+^{120}Sn$	2.468	1.92(2)	1.560(5)	[49,53]
$^{10}B+^{120}Sn$	4.461	1.83(3)	1.538(3)	[48,55]
$^{11}B+^{120}Sn$	8.664	1.78(2)	1.551(3)	[56]
$^{12}C+^{120}Sn$	7.275	1.86(7)	1.549(3)	This work
$^{12}C+^{119}Sn$	7.275	1.80(3)	1.534(3)	[34]
$^{16}O+^{120}Sn$	7.162	1.71(2)	1.539(2)	[57]

where Z_p and Z_T represent, respectively, the atomic number of projectile and target.

The reduced distance of the closest approach can be defined by $d = D/(A_p^{1/3} + A_T^{1/3})$, where A_p and A_T represent, respectively, the atomic mass of the projectile and target. This avoids geometrical differences and enables a direct comparison between different systems.

Figure 14 shows the ratio of elastic scattering to Rutherford cross section (σ_{el}/σ_R) as a function of d for $^{12}C+^{120}Sn$ data (this work), compared to several other projectiles (^{6}He [52], ^{6}Li [31], ^{7}Li [49,53], ^{9}Be [54], $^{10,11}B$ [48,55,56], and ^{16}O [57]) reacting on the same target. For comparisons, Fig. 14 also shows the results for $^{12}C+^{208}Pb$ [58,59] and $^{12}C+^{119}Sn$ [34].

In Fig. 14, the experimental elastic scattering cross sections (σ_{el}/σ_R) are fitted by a Boltzmann-type exponential function as in Ref. [50], which is given by

$$\frac{\sigma_{el}}{\sigma_R} = \frac{p_1}{1 + e^{d_1(d-d_2)}}, \quad (7)$$

where p_1, d_1, and d_2 are its parameters. The critical interaction distance (d_I) and the reduced strong absorption distance (d_S) have been defined as those for which this fitting function decreases, respectively, by the factors 0.98 and 0.25 of its maximum value (p_1) [50,60].

Tables VII and VIII present the distances d_I and d_S for different projectiles that react with the ^{120}Sn and ^{208}Pb targets. Our calculations of d_I and d_S are compatible with those originally presented [50,51,61]. As can be seen, all projectiles have a quite similar d_S, whereas d_I better reveals their features.

TABLE VIII. Calculated reduced critical interaction d_I and the reduced strong-absorption d_S distances presented in Ref. [50], for tightly and weakly bound projectiles reacting on ^{208}Pb.

System	Q_{bu} (MeV)	d_I (fm)	d_S (fm)	Ref.
$^{11}Li+^{208}Pb$	0.369	5.2(4)	1.59(4)	[62]
$^{6}He+^{208}Pb$	0.975	2.20(5)	1.589(7)	[63]
$^{6}Li+^{208}Pb$	1.474	1.95(4)	1.521(5)	[64]
$^{9}Be+^{208}Pb$	1.655	1.86(2)	1.540(4)	[65]
$^{7}Li+^{208}Pb$	2.468	1.74(2)	1.491(3)	[64]
$^{12}C+^{208}Pb$	7.275	1.66(1)	1.491(2)	[58]
$^{16}O+^{208}Pb$	7.162	1.64(1)	1.498(2)	[66]

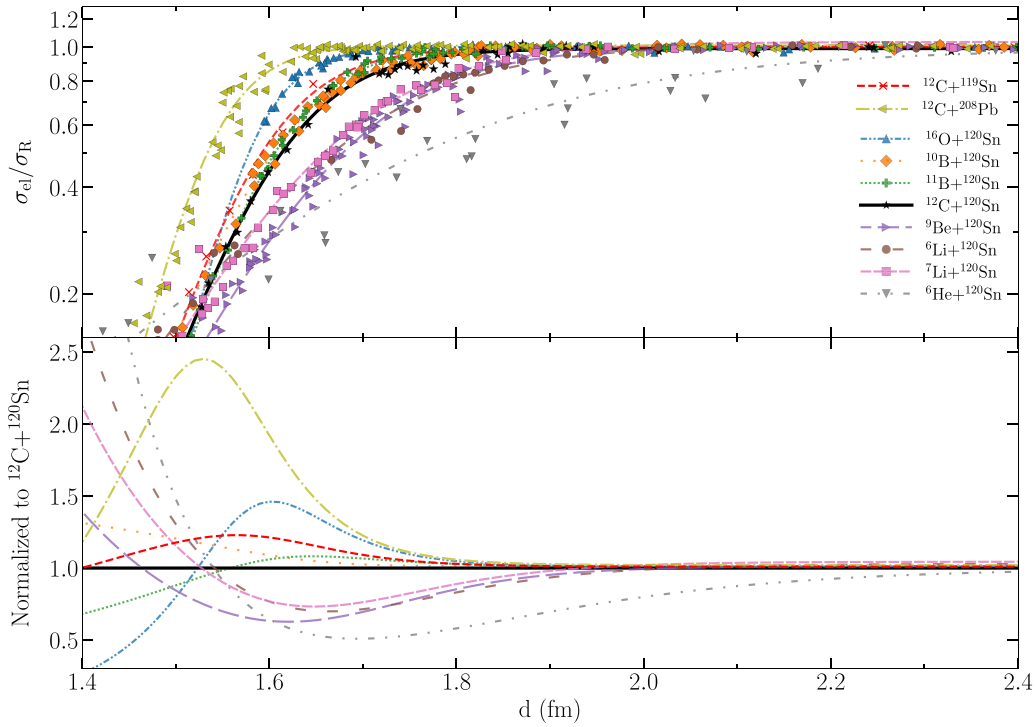

FIG. 14. Ratio of the elastic scattering to Rutherford cross section versus the reduced distance of closest approach. The curves represent the fit given by Eq. (7) to the data. This figure shows a zoom-in of the region between the reduced critical interaction d_I and the reduced strong-absorption d_S distances. In the lower panel, the fits are normalized to the σ_{el}/σ_R related to the $^{12}C + ^{120}Sn$ (horizontal solid black line) in this region of interest. References are indicated in the text.

From Tables VII and VIII, the distance d_I tends to be shorter in the case of tightly bound projectiles, such as $^{10,11}B$, ^{12}C and ^{16}O; it increases for weakly bound projectiles, such as $^{6,7}Li$ and ^{9}Be; and increases even more for reactions with exotic nuclei, such as ^{11}Li and ^{6}He.

In Fig. 14, the lower panel represents the ratio of σ_{el}/σ_R for each system normalized to the $^{12}C + ^{120}Sn$ case (horizontal solid black line). Thus, above the solid line, we have σ_{el}/σ_R for $^{10,11}B$, $^{16}O + ^{120}Sn$, $^{12}C + ^{208}Pb$, and $^{12}C + ^{119}Sn$. This means that the σ_{el} for these systems decreases from Rutherford at a shorter distance than the one for $^{12}C + ^{120}Sn$. Below the solid line, we have σ_{el}/σ_R for $^{6,7}Li$, ^{9}Be, and $^{6}He + ^{120}Sn$, suggesting that the σ_{el} for these systems decreases from Rutherford at larger distances than the one for $^{12}C + ^{120}Sn$. The $^{6}He + ^{120}Sn$ represents one extreme case, where the deviation from Rutherford begins much further away. This is in agreement with the results presented in Refs. [33,63,67–69]. The results obtained for $^{6,7}Li$, ^{9}Be, and ^{6}He contrast with the results of $^{10,11}B$ and ^{12}C projectiles in interaction with ^{120}Sn target. For instance, in the case of ^{10}B, significantly lower absorption (represented by lower $N_i \sim 0.35$ values) have been reported [31]. This can be correlated with the higher fusion cross section obtained for ^{10}B compared to other projectiles [70]. Thus, fusion tends to prevail for $^{10,11}B$ and ^{12}C, while the peripheral reaction process seems to dominate for stable weakly bound nuclei, such as $^{6,7}Li$, ^{9}Be, and exotic nuclei such as ^{6}He.

Thus, comparing the region between the distances d_I and d_S, for different systems, we can differentiate the reaction dynamics of ^{12}C from the others. In addition, we differentiate between the reactions of stable tightly bound and weakly bound nuclei, and the reactions of stable and exotic nuclei, with the characteristic long-range absorption processes of the latter [33,63,67–69].

VI. SUMMARY AND CONCLUSIONS

This manuscript presents new experimental data and theoretical calculations for the elastic scattering angular distributions of $^{12}C + ^{120}Sn$ and the following nuclear reaction channels: inelastic excitations to the 2^+ state at 1171.27(2) keV and to the 3^- state at 2400.30(5) keV of the ^{120}Sn target, ^{12}C one-proton stripping $^{120}Sn(^{12}C, ^{11}B)\,^{121}Sb$ and one-neutron pickup $^{120}Sn(^{12}C, ^{13}C)\,^{119}Sn$ transfer reactions.

We analyze the experimental data using the SP-OMP and CC and CRC calculations. The calculations provide an overall description of the data.

Low-energy data analysis, close to the Coulomb barrier, is known to be sensitive to the nuclear potential surface region around the so-called strong absorption radius [16]. However, for the $^{12}C + ^{120}Sn$ case, the data obtained at 38.7 MeV (below the Coulomb barrier) show little sensitivity to the real OP term. We observe that the data fit is mostly sensitive to the imaginary OP term. This sensitivity does not correlate with barrier penetration (since it is not considered by OM1 and its respective internal absorption). Instead, it correlates with the peripheral reaction channels (inelastic excitation and nucleon transfers), observed in the experimental spectra, and the respective surface absorption, which is better accounted for by OM2, OM3 and OM4. In Ref. [71], the authors question

whether the unusual near-threshold potential behavior, observed in the elastic scattering of weakly bound nuclei, could be related to a precision error. In addition, the authors claim that uncertainty quantification of elastic scattering data with a physical constraint of the imaginary part of the OP is needed to extract the OP from the data. The reaction channels (observed at our spectra) are, indeed, the main physical constraint to the imaginary part of OP. Thus, they have been analyzed through microscopic CC calculations.

In general, the results obtained for the $^{12}C + ^{120}Sn$ data are consistent with previous systematic work on reactions involving tightly and weakly bound nuclei [29,31,32].

We compare the elastic scattering angular distributions of $^{12}C + ^{119}Sn$ [34] with $^{12}C + ^{120}Sn$ ones (this work). In both cases, the combination of OM1 (internal absorption) with CC calculations describe the experimental data quite consistently.

The CRC calculations, using the SPP as the bare interaction, provide an overall description of the $^{12}C + ^{119,120}Sn$ experimental angular distributions. These calculations were performed applying an imaginary WS shape potential (OM1), with a set of fixed parameters that result in internal flux absorption and negligible strength in the surface region.

In both $^{12}C + ^{119,120}Sn$ cases, we verified that the transfer couplings effect on the elastic scattering angular distribution (and other channels) is negligible.

As in the case of $^{12}C + ^{119}Sn$, we have studied the effect of coupling inelastic excitations to the ^{12}C 2^+ and 3^- states, at 4439.8(2) and 9641(5) keV. The CRC calculations show that these effects are not negligible, and their couplings help to describe the experimental data set.

In the $^{12}C + ^{120}Sn$ reactions, the specific main inelastic excitations to the ^{120}Sn 2^+ state, at 1171.27(2) keV and the 3^- state, at 2400.30(5) keV were considered in the coupling scheme, providing an overall agreement with the experimental data set. Unlike ^{120}Sn, in the case of ^{119}Sn, experimental cross sections involve contributions from multiple excited states of the residual nuclei. In particular, couplings associated with the excitation of states near 2.30 MeV were experimentally observed and showed a significant effect on the elastic scattering description. In this energy region, a complete CRC calculation, considering all possible excited states, is impractical. Thus, the corresponding theoretical cross sections were obtained using a simplified coupling scheme, where a single state $5/2^+$ ^{119}Sn, with $E^* = 2.30$ MeV, was adopted to simulate the effect of nearby populated excited states of the ^{119}Sn. The Coulomb and nuclear deformation parameters were varied to match the corresponding experimental cross sections.

These results provide another important reference for comparison purposes and contribute to a common description of stable reactions of tightly and weakly bound nuclei [31,32]. As an example, we compare the elastic cross section (σ_{el}/σ_R) as a function of the reduced distance of the closest approach (d), for the ^{12}C data (this work), compared to several other projectiles interacting with three different targets ($^{119,120}Sn$ and ^{208}Pb). This reduced distance of closest approach allows us, in a very simple way, to differentiate when reaction channels are initiated, according to the nuclei involved. Despite its simplicity, it clearly differentiates ^{12}C from other projectiles reacting on ^{120}Sn and from the same ^{12}C projectile reacting on two different isotopes ($^{119,120}Sn$). In addition, it also differentiates between exotic and stable (tightly and weakly bound) nuclei reactions. Comparisons with a third target (^{208}Pb) are presented.

The determined OP served as a valuable benchmark for analyzing additional nuclear reaction processes. In particular, the OP was used as the initial interaction to study the angular distributions of inelastic excitations and nucleon transfer reactions from coupled-channel calculations.

ACKNOWLEDGMENTS

The financial support from the Argentinean FONCyT (Fondo para la Investigación Cientfica y Tecnológica) through Grant No. (PICT-2019-3565) is acknowledged. This work has been partially supported by the Coordenação de Aperfeiçoamento de Pessoal de Nível Superior (CAPES) Proc. No. 88887.834953/2023-00, Fundação de Amparo à Pesquisa do Estado de São Paulo (FAPESP) Proc. No. 2019/07767-1, 2021/11425-9, 2022/09060-5, 2024/01416-0, Conselho Nacional de Desenvolvimento Científico e Tecnológico (CNPq) Proc. No. 302544/2022- 4, 302072/2022-5, 315864/2023-0, and Project INCT-FNA Proc. No. 464898/2014-5. This work has also been partially supported by the Spanish Ministerio de Economía y Competitividad and FEDER funds (Grant No. PGC2018-096994-B-C21) by Project PAIDI 2020, Reference No. P20_01247, funded by the Consejería de Economía, Conocimiento, Empresas y Universidad, Junta de Andalucía (Spain) and "ERDF A way of making Europe," and Ministerio de Universidades (Grant No. REC-B-22289-1/2). This work is also part of the project supported by the Spanish Ministerio de Ciencia, Innovación y Universidades (Grant No. PID2023-146401NB-I00). Finally, this work has been developed within the context of IReNA (*International Research Network for Nuclear Astrophysics*) and IANNA (*Ibero-American Network of Nuclear Astrophysics*). The authors acknowledge support and collaboration from IReNA and IANNA (National Science Foundation under Grant No. OISE-1927130).

DATA AVAILABILITY

The data that support the findings of this article are not publicly available. The data are available from the authors upon reasonable request.

[1] National Nuclear Data Center, NuDat database, www.nndc.bnl.gov/nudat3/.
[2] F. Hoyle, Astrophys. J. Suppl. Series **1**, 121 (1954).
[3] C. W. Cook, W. A. Fowler, C. C. Lauritsen, and T. Lauritsen, Phys. Rev. **107**, 508 (1957).
[4] M. Freer and H. Fynbo, Prog. Part. Nucl. Phys. **78**, 1 (2014).
[5] K. Kitao, Y. Tendow, and A. Hashizume, Nucl. Data Sheets **96**, 241 (2002).
[6] H. Feshbach, C. E. Porter, and V. F. Weisskopf, Phys. Rev. **96**, 448 (1954).
[7] H. Feshbach, Ann. Phys. **5**, 357 (1958).
[8] G. Satchler and W. Love, Phys. Lett. B **76**, 23 (1978).

[9] G. Satchler, Phys. Lett. B **83**, 284 (1979).
[10] G. Satchler and W. Love, Phys. Rep. **55**, 183 (1979).
[11] J. Cook, Nucl. Phys. A **388**, 153 (1982).
[12] G. Satchler, Phys. Rep. **199**, 147 (1991).
[13] D. T. Khoa, W. von Oertzen, and H. G. Bohlen, Phys. Rev. C **49**, 1652 (1994).
[14] D. T. Khoa, G. R. Satchler, and W. von Oertzen, Phys. Rev. C **51**, 2069 (1995).
[15] D. T. Khoa and G. Satchler, Nucl. Phys. A **668**, 3 (2000).
[16] M. Brandan and G. Satchler, Phys. Rep. **285**, 143 (1997).
[17] R. Varner, W. Thompson, T. McAbee, E. Ludwig, and T. Clegg, Phys. Rep. **201**, 57 (1991).
[18] C. Hebborn, F. M. Nunes, G. Potel, W. H. Dickhoff, J. W. Holt, M. C. Atkinson, R. B. Baker, C. Barbieri, G. Blanchon, M. Burrows, R. Capote, P. Danielewicz, M. Dupuis, C. Elster, J. E. Escher, L. Hlophe, A. Idini, H. Jayatissa, B. P. Kay, K. Kravvaris *et al.*, J. Phys. G: Nucl. Part. Phys. **50**, 060501 (2023).
[19] M. S. Hussein, P. R. S. Gomes, J. Lubian, and L. C. Chamon, Phys. Rev. C **73**, 044610 (2006).
[20] J. F. Niello, J. Figueira, D. Abriola, A. Arazi, O. Capurro, G. Martí, D. M. Heinmann, A. Pacheco, E. de Barbará, I. Padrón, P. Gomes, and J. Lubian, Nucl. Phys. A **787**, 484 (2007).
[21] M. Zadro, P. Figuera, A. Di Pietro, F. Amorini, M. Fisichella, O. Goryunov, M. Lattuada, C. Maiolino, A. Musumarra, V. Ostashko, M. Papa, M. G. Pellegriti, F. Rizzo, D. Santonocito, V. Scuderi, and D. Torresi, Phys. Rev. C **80**, 064610 (2009).
[22] N. N. Deshmukh, S. Mukherjee, D. Patel, N. L. Singh, P. K. Rath, B. K. Nayak, D. C. Biswas, S. Santra, E. T. Mirgule, L. S. Danu, Y. K. Gupta, A. Saxena, R. K. Choudhury, R. Kumar, J. Lubian, C. C. Lopes, E. N. Cardozo, and P. R. S. Gomes, Phys. Rev. C **83**, 024607 (2011).
[23] F. Gollan, D. Abriola, A. Arazi, O. Capurro, M. Cardona, E. de Barbará, D. Hojman, G. Martí, A. Pacheco, D. Rodrigues, and J. Testoni, Nucl. Phys. A **979**, 87 (2018).
[24] L. C. Chamon, B. V. Carlson, L. R. Gasques, D. Pereira, C. De Conti, M. A. G. Alvarez, M. S. Hussein, M. A. Cândido Ribeiro, E. S. Rossi, and C. P. Silva, Phys. Rev. C **66**, 014610 (2002).
[25] M. A. Cândido Ribeiro, L. C. Chamon, D. Pereira, M. S. Hussein, and D. Galetti, Phys. Rev. Lett. **78**, 3270 (1997).
[26] L. C. Chamon, D. Pereira, M. S. Hussein, M. A. Cândido Ribeiro, and D. Galetti, Phys. Rev. Lett. **79**, 5218 (1997).
[27] L. C. Chamon, D. Pereira, and M. S. Hussein, Phys. Rev. C **58**, 576 (1998).
[28] D. Galetti, S. S. Mizrahi, L. C. Chamon, D. Pereira, M. S. Hussein, and M. A. C. Ribeiro, Phys. Rev. C **58**, 1627 (1998).
[29] M. A. G. Alvarez, L. C. Chamon, M. S. Hussein, D. Pereira, L. R. Gasques, E. S. Rossi, and C. P. Silva, Nucl. Phys. A **723**, 93 (2003).
[30] M. A. G. Alvarez, N. Alamanos, L. C. Chamon, and M. S. Hussein, Nucl. Phys. A **753**, 83 (2005).
[31] M. A. G. Alvarez, J. P. Fernández-García, J. L. León-García, M. Rodríguez-Gallardo, L. R. Gasques, L. C. Chamon, V. A. B. Zagatto, A. Lépine-Szily, J. R. B. Oliveira, V. Scarduelli, B. V. Carlson, J. Casal, A. Arazi, D. A. Torres, and F. Ramirez, Phys. Rev. C **100**, 064602 (2019).
[32] L. Garrido-Gómez, A. Vegas-Díaz, J. Fernández-García, and M. Alvarez, Phys. Rev. C **109**, 054608 (2024).
[33] M. A. G. Alvarez, M. Rodríguez-Gallardo, J. P. Fernández-García, J. Casal, and J. A. Lay, Phys. Rev. C **103**, 054614 (2021).
[34] L. M. Martinis, L. R. Gasques, J. P. Fernández-García, V. Scarduelli, M. A. G. Alvarez, L. C. Chamon, W. A. Y. Hatano, J. K. L. Chaves, G. P. Cessel, and L. Garrido-Gómez, Phys. Rev. C **111**, 034615 (2025).
[35] L. Chamon, B. Carlson, and L. Gasques, Comput. Phys. Commun. **267**, 108061 (2021).
[36] B. V. Carlson and D. Hirata, Phys. Rev. C **62**, 054310 (2000).
[37] H. De Vries, C. De Jager, and C. De Vries, At. Data Nucl. Data Tables **36**, 495 (1987).
[38] I. J. Thompson, Comput. Phys. Rep. **7**, 167 (1988).
[39] D. Abriola, A. Arazi, J. Testoni, F. Gollan, and G. V. Martí, J. Phys.: Conf. Ser. **630**, 012021 (2015).
[40] S. Cohen and D. Kurath, Nucl. Phys. A **101**, 1 (1967).
[41] M. Febbraro, F. D. Becchetti, R. O. Torres-Isea, J. Riggins, C. C. Lawrence, J. J. Kolata, and A. M. Howard, Phys. Rev. C **96**, 024613 (2017).
[42] X. D. Liu, M. A. Famiano, W. G. Lynch, M. B. Tsang, and J. A. Tostevin, Phys. Rev. C **69**, 064313 (2004).
[43] D. F. M. Botero, L. C. Chamon, and B. V. Carlson, J. Phys. G: Nucl. Part. Phys. **44**, 105102 (2017).
[44] L. Chamon and B. Carlson, Nucl. Phys. A **846**, 1 (2010).
[45] B. Pritychenko, M. Birch, B. Singh, and M. Horoi, At. Data Nucl. Data Tables **107**, 1 (2016).
[46] T. Kibedi and R. Spear, At. Data Nucl. Data Tables **80**, 35 (2002).
[47] L. R. Gasques, M. A. G. Alvarez, A. Arazi, B. V. Carlson, L. C. Chamon, J. P. Fernández-García, A. Lépine-Szily, J. Lubian, J. Rangel, M. Rodríguez-Gallardo, V. Scarduelli, and V. A. B. Zagatto, Phys. Rev. C **103**, 034616 (2021).
[48] L. R. Gasques, A. S. Freitas, L. C. Chamon, J. R. B. Oliveira, N. H. Medina, V. Scarduelli, E. S. Rossi, M. A. G. Alvarez, V. A. B. Zagatto, J. Lubian, G. P. A. Nobre, I. Padron, and B. V. Carlson, Phys. Rev. C **97**, 034629 (2018).
[49] A. Kundu, S. Santra, A. Pal, D. Chattopadhyay, R. Tripathi, B. J. Roy, T. N. Nag, B. K. Nayak, A. Saxena, and S. Kailas, Phys. Rev. C **95**, 034615 (2017).
[50] V. Guimarães, J. Lubian, J. J. Kolata, E. F. Aguilera, M. Assunção, and V. Morcelle, Eur. Phys. J. A **54**, 223 (2018).
[51] V. Guimarães, P. C. Nistal, S. D. Olorunfunmi, R. Linares, and J. Lubian, Front. Phys. **13**, 1518626 (2025).
[52] P. Mohr, P. N. de Faria, R. Lichtenthäler, K. C. C. Pires, V. Guimarães, A. Lépine-Szily, D. R. Mendes, A. Arazi, A. Barioni, V. Morcelle, and M. C. Morais, Phys. Rev. C **82**, 044606 (2010).
[53] V. A. B. Zagatto, J. Lubian, L. R. Gasques, M. A. G. Alvarez, L. C. Chamon, J. R. B. Oliveira, J. A. Alcántara-Núñez, N. H. Medina, V. Scarduelli, A. Freitas, I. Padron, E. S. Rossi, and J. M. B. Shorto, Phys. Rev. C **95**, 064614 (2017).
[54] A. Arazi, J. Casal, M. Rodríguez-Gallardo, J. M. Arias, R. Lichtenthäler Filho, D. Abriola, O. A. Capurro, M. A. Cardona, P. F. F. Carnelli, E. de Barbará, J. Fernández Niello, J. M. Figueira, L. Fimiani, D. Hojman, G. V. Martí, D. Martínez Heimman, and A. J. Pacheco, Phys. Rev. C **97**, 044609 (2018).
[55] M. A. G. Alvarez, M. Rodríguez-Gallardo, L. R. Gasques, L. C. Chamon, J. R. B. Oliveira, V. Scarduelli, A. S. Freitas, E. S. Rossi, V. A. B. Zagatto, J. Rangel, J. Lubian, and I. Padron, Phys. Rev. C **98**, 024621 (2018).
[56] V. Scarduelli, L. R. Gasques, L. C. Chamon, V. A. B. Zagatto, M. A. G. Alvarez, and A. Lépine-Szily, Phys. Rev. C **106**, 044606 (2022).

[57] C. Silva, M. Alvarez, L. Chamon, D. Pereira, M. Rao, E. Rossi Jr., L. Gasques, M. Santo, R. Anjos, J. Lubian, P. Gomes, C. Muri, B. Carlson, S. Kailas, A. Chatterjee, P. Singh, A. Shrivastava, K. Mahata, and S. Santra, Nucl. Phys. A **679**, 287 (2001).

[58] S. Santra, P. Singh, S. Kailas, A. Chatterjee, A. Shrivastava, and K. Mahata, Phys. Rev. C **64**, 024602 (2001).

[59] P. L. D. Magro, V. Guimarães, M. Assunção, E. O. N. Zevallos, M. B. Angelo, L. M. Garcia-Figueroa, F. Miletto, A. Arazi, D. Hojman, M. A. Cardona, E. de Barbará, J. Gomez, B. Paes, E. N. Cardozo, J. Lubian, and J. C. Zamora, Eur. Phys. J. A **60**, 122 (2024).

[60] A. Pakou and K. Rusek, Phys. Rev. C **69**, 057602 (2004).

[61] A. Pakou, O. Sgouros, V. Soukeras, J. Casal, and K. Rusek, Eur. Phys. J. A **58**, 8 (2022).

[62] M. Cubero, J. P. Fernández-García, M. Rodríguez-Gallardo, L. Acosta, M. Alcorta, M. A. G. Alvarez, M. J. G. Borge, L. Buchmann, C. A. Diget, H. A. Falou, B. R. Fulton, H. O. U. Fynbo, D. Galaviz, J. Gómez-Camacho, R. Kanungo, J. A. Lay, M. Madurga, I. Martel, A. M. Moro, I. Mukha *et al.*, Phys. Rev. Lett. **109**, 262701 (2012).

[63] A. Sánchez-Benítez, D. Escrig, M. Álvarez, M. Andrés, C. Angulo, M. Borge, J. Cabrera, S. Cherubini, P. Demaret, J. Espino, P. Figuera, M. Freer, J. García-Ramos, J. Gómez-Camacho, M. Gulino, O. Kakuee, I. Martel, C. Metelko, A. Moro, F. Pérez-Bernal *et al.*, Nucl. Phys. A **803**, 30 (2008).

[64] N. Keeley, S. Bennett, N. Clarke, B. Fulton, G. Tungate, P. Drumm, M. Nagarajan, and J. Lilley, Nucl. Phys. A **571**, 326 (1994).

[65] N. Yu, H. Q. Zhang, H. M. Jia, S. T. Zhang, M. Ruan, F. Yang, Z. D. Wu, X. X. Xu, and C. L. Bai, J. Phys. G: Nucl. Part. Phys. **37**, 075108 (2010).

[66] E. Vulgaris, L. Grodzins, S. G. Steadman, and R. Ledoux, Phys. Rev. C **33**, 2017 (1986).

[67] J. Fernández-García, M. Rodríguez-Gallardo, M. Alvarez, and A. Moro, Nucl. Phys. A **840**, 19 (2010).

[68] J. Fernández-García, M. Alvarez, A. Moro, and M. Rodríguez-Gallardo, Phys. Lett. B **693**, 310 (2010).

[69] J. P. Fernández-García, M. A. G. Alvarez, and L. C. Chamon, Phys. Rev. C **92**, 014604 (2015).

[70] M. Aversa, D. Abriola, M. A. G. Alvarez, A. Arazi, M. A. Cardona, L. C. Chamon, E. de Barbará, J. de Jesús, J. P. Fernández-García, L. R. Gasques, D. Hojman, A. Lépine-Szily, G. V. Martí, A. J. Pacheco, V. Scarduelli, and V. A. B. Zagatto, Phys. Rev. C **101**, 044601 (2020).

[71] R. N. Pérez and J. Lei, Phys. Lett. B **795**, 200 (2019).